EUR Research Information Portal

Higher-order Singular Value Decomposition Filter for Contrast Echocardiography

Document Version
Publisher's PDF, also known as Version of record

Citation for the published version (APA):
Wahyulaksana, G., Wei, L., Voorneveld, J., Hekkert, M. T. L., Strachinaru, M., Duncker, D. J., De Jong, N., Van der Steen, A. F. W., & Vos, H. J. (2023). Higher-order Singular Value Decomposition Filter for Contrast Echocardiography. *IEEE Transactions on Ultrasonics, Ferroelectrics, and Frequency Control*, *70*(11), 1371-1383. https://doi.org/10.1109/tuffc.2023.3316130

Link to publication on the EUR Research Information Portal

Erasmus University Rotterdam
Making Minds Matter

Higher-order Singular Value Decomposition Filter for Contrast Echocardiography

Geraldi Wahyulaksana, Luxi Wei, Jason Voorneveld, Maaike te Lintel Hekkert, Mihai Strachinaru, Dirk J. Duncker, Nico de Jong, Antonius F.W. van der Steen, Hendrik J. Vos

Abstract—**Assessing the coronary circulation with contrast-enhanced echocardiography has high clinical relevance. However, it is not being routinely performed in clinical practice because the current clinical tools generally could not provide adequate image quality. The contrast agent's visibility in the myocardium is generally poor, impaired by motion and non-linear propagation artifacts. The established multi-pulse contrast schemes (MPCS) and the more experimental singular value decomposition (SVD) filter also fall short to solve these issues. Here, we propose a scheme to process AM/AMPI echoes with higher-order singular value decomposition (HOSVD) instead of conventionally summing the complementary pulses. The echoes from the complementary pulses form a separate dimension in the HOSVD algorithm. Then, removing the ranks in that dimension with dominant coherent signals coming from tissue scattering would provide the contrast detection. We performed both *in vitro* and *in vivo* experiments to assess the performance of our proposed method in comparison with the current standard methods. A flow phantom study shows that HOSVD on AM pulsing exceeds the contrast-to-background ratio (CBR) of conventional AM and an SVD filter by 10dB and 14dB, respectively. *In vivo* porcine heart results also demonstrate that, compared to AM, HOSVD improves CBR in open-chest acquisition (up to 19dB) and contrast ratio in closed-chest acquisition (3dB).**

Index Terms— **contrast-enhanced ultrasound, ultrafast imaging, higher-order singular value decomposition (HOSVD), microbubble detection, myocardial perfusion**

I. INTRODUCTION

Contrast echocardiography (CE) is a clinically established diagnostic tool for assessing the ejection fraction and regional wall motion, when image quality is poor in regular B-mode imaging [1], [2]. Signal strength of the blood pool and vasculature are enhanced using ultrasound contrast agents (UCA), consisting of micron-sized lipid-coated gas bubbles that are injected intravenously [3]. CE can also be used to assess myocardial perfusion. However, accurate and reliable perfusion imaging has been a challenge since its introduction. The shadowing from the ribs and lungs, attenuation of signal due to the contrast agent in the cardiac cavities, noise, and strong clutter signal originating from stationary and moving tissue are contributing factors that lead to limited image quality [3], [4].

In the past decades, several contrast-specific pulsing schemes have been developed to suppress tissue clutter signal and provide the contrast detection. Generally, two categories can be distinguished. One category relies solely on the generation of harmonic signals due to nonlinear scattering of ultrasound by the microbubbles. In these schemes, sub or higher harmonics of the originally transmitted ultrasound frequency would be selectively retained to show the contrast agents on screen. Yet, it was found that tissue also generates harmonic frequency content by nonlinear propagation, thus leading to substantial tissue clutter [5]. The other category is contrast pulsing schemes that relies on sending multiple pulses that suppress the linear tissue clutter signal when the echoes are combined by simple subtraction or addition, sometimes after scalar multiplication. The most commonly used multi-pulse contrast schemes (MPCS) are pulse inversion (PI) [6], amplitude modulation (AM) [7], and their combination, i.e., amplitude modulated pulse inversion (AMPI) [8]. However, as ultrasound also propagates nonlinearly when it travels through tissue or a microbubble cloud, the tissue suppression effectiveness is reduced as well for these schemes. This might be significant for cardiac imaging where the chambers are filled with microbubbles following intravenous administration and the nonlinearity is substantially accumulated due to great imaging depth, which would lead to the unwanted 'nonlinear' tissue signal again [9]. Moreover, the rapid myocardial motion throughout the cardiac cycle causes out-of-phase summation of the linear components from multiple transmission, which are therefore not fully suppressed. This again results in tissue clutter through so-called motion artifacts [10], [11].

Another approach to suppress the tissue clutter signal is by using a post-processing clutter filter. Originally, the clutter filtering is performed as frequency filters on a packet of consecutive frames with the assumption that blood flow and tissue motion have distinct spectral characteristics in such ensembles. However, that assumption is not valid when the

flow velocity and tissue motion have overlapping spectral content [12], which is generally the case in microvascular myocardial perfusion imaging. More recently, the advancement of high-frame-rate (HFR) ultrasound imaging [13] provides highly coherent data in both space and time that facilitates clutter filtering using spatiotemporal information. High frame rate contrast-enhanced ultrasound (HFR-CEUS) combined with singular value decomposition (SVD) filtering [14] has been used ubiquitously in research setting to reduce tissue clutter enabling assessment of flow in the vasculature. SVD decomposes the tissue, blood flow, and noise into separate singular vectors, assuming they have different spatiotemporal coherence. Ideally, the filtering process is then performed by removing tissue and noise singular vectors, with only the flow signal of the interest remaining. It has been reported that SVD suppresses tissue clutter better than conventional frequency filters and contrast pulsing schemes (AM and AMPI) [14]–[16]. However, its performance also degrades with slower flow rates and faster tissue motion since in that case the coherence between the contrast agent signal and tissue increases, thus preventing the separation into different components [14], [17], [18]. This is a crucial issue for cardiac imaging where tissue motion can reach up to 9.4 cm/s [19] and blood flow in the microcirculation is generally slower than 1 cm/s. To mitigate this problem, the combination of SVD and AM by applying SVD on AM-processed images was attempted. However, it has been reported that it achieves lower contrast-to-background ratio than an SVD filter alone [16]. In this case, the SVD filter fails to improve contrast detection of the AM-processed images because it operates in the spatiotemporal dimension, where the residual tissue and microbubble signal are highly coherent and of same order of magnitude in strength.

To achieve better tissue and contrast separation, we propose to expand the filter operating dimensions by using higher-order singular value decomposition (HOSVD), instead of using 'regular' SVD that can only take a 2-dimensional matrix as input. It is a multilinear generalization of SVD, in which HOSVD decomposes an nth order tensor [20]. Its usage to improve blood flow visualization in medical ultrasound imaging has been proposed by Kim *et al.* [21]. They demonstrated that using Doppler frames as the third dimension could improve blood flow and perfusion separation from tissue clutter. However, their implementation is aimed at tissue with slow motion and without exploiting the nonlinear property of UCAs.

We expect that HOSVD can improve MPCS performance to detect UCAs if the underlying structure of the data meets the assumptions attained in the decomposition. In this study, we propose using HOSVD to combine the received echoes from the complementary pulses in the multi-pulse contrast schemes, instead of the conventional linear signal combinations. In the case of MPCS, it is assumed that contrast agents respond nonlinearly to the ultrasound pulses whereas tissue response is mostly linear. Thus, we can add the pulsing sequence as a third dimension to the spatial and temporal information. We hypothesize that the nonlinear part of the microbubble signal would be decomposed into different components than the tissue

clutter signal, after which data separation can be performed by appropriate component selection. An *in vitro* measurement with a flow phantom as well as *in vivo* cardiac measurement were performed to assess the efficacy of our proposed method. The performance of our proposed technique will be evaluated and compared with the conventionally processed MPCS and the regular spatiotemporal SVD filter.

II. MATERIALS AND METHODS

A. In vitro setup

We built an in-vitro setup that could emulate rigid tissue motion and the effect of nonlinear propagation through a cloud of bubbles. A tissue-mimicking wall-less flow phantom was made from a suspension of 10% w/v polyvinyl alcohol (PVA) and 1% w/v silicon carbide as background scattering particles, 20% cooling liquid, and 69% distilled water with one completed freeze-thaw thermal cycle, see Fig. 1. To obtain ultrasound images in the presence of nonlinear propagation through a bubble cloud, diluted Definity (Lantheus Medical Imaging, North Billerica, MA) with a concentration of ~0.5 – 1.1 x 10^6 MB/mL were put into the phantom chamber on top. The same dilution was infused with a perfusion pump through a 1-mm diameter channel as the microbubbles of interest. Since the minimum flow that this syringe pump could provide was 6 mm/s, we turned off the pump to have negligible flow, thus mimicking capillary perfusion rather than vascular flow. An ultrasound probe (see Fig. 1.) was attached to a linear stage. Rigid tissue motion was emulated by moving the probe in vertical direction during image acquisition. The peak velocity of the probe was 35 mm/s that emulates the peak velocity of the left main coronary artery environment [22].
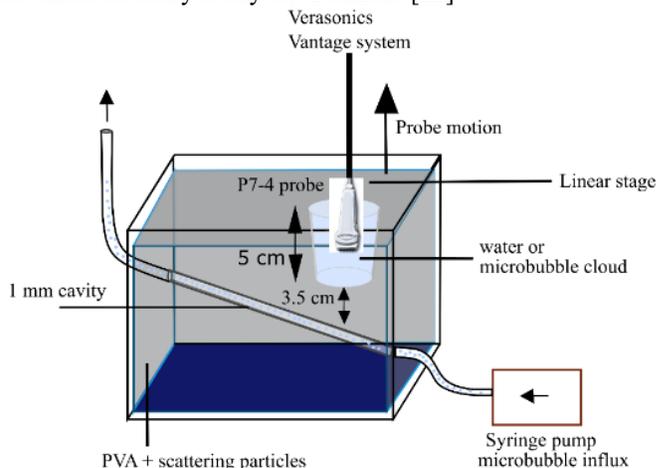
Fig. 1. Setup of the flow phantom. The probe was positioned inside the chamber to emulate both rigid tissue motion and nonlinear propagation through microbubble cloud.

B. In vivo porcine myocardial perfusion model

Two female Yorkshire x Norwegian Landrace porcine (35 and 38 kg) experiments followed European Union and institutional guidelines for the care and use of laboratory animals, with CCD approval AVD1010020172411 (SP2100125). They were first sedated, put under full anaesthesia using pentobarbital (10-15 mg/kg/h) and

mechanically vented. Animals were positioned in a supine position. Vital signs were monitored. A diluted (30x) Definity® solution (Lantheus Medical Imaging Inc., MA, USA) was continuously infused through the jugular vein at 1.5 ml/min. The acquisitions were performed both trans-thoracically (closed-chest), and by direct cardiac access after sternotomy (open-chest).

C. Ultrasound transmission and beamforming

Radio frequency acquisitions in both *in vitro* and *in vivo* experiments were performed with a 64-element phased array transducer (P7-4, Philips ATL, Bothell, WA), connected to a Vantage 256 system (Verasonics Inc., Redmond, WA). The high-frame-rate (HFR) imaging was performed with diverging waves with a pulse repetition frequency of 4.5 kHz, center frequency of 5.2 MHz (3 cycles), and image depth of 10 cm. Multi-pulse contrast sequences (AM and AMPI) were adopted on the fundamental frequency (non-linear fundamental imaging)[8]. AM was used in the *in vitro* measurement. Both AM and AMPI transmission schemes were used in *in vivo* experiments. The *in vitro* HFR transmission sequence only consisted of one transmit aperture (64 elements) with final frame rate of 1500 Hz. In the *in vivo* experiment, an acquisition consisted of 1s of HFR recordings, a high mechanical index (MI) focused beam "FLASH" microbubble destruction sequence, and a subsequent 4s of HFR recordings. The *in vivo* HFR transmission sequence consisted of 3 synthetic transmit apertures (21 elements each) with overlapping beams to increase spatial resolution with coherent compounding [23] and final frame rate of 500 Hz. The 'checkerboard pattern' with even, full, and odd element number transmission was completed per sub-aperture. The 'FLASH' destruction sequence consisted of transmitting 21 cycles focused beam with MI ≈ 1. Channel data were beamformed offline using the Ultrasound Toolbox [24] in Matlab (R2022A, the Mathworks, Natick, 2022) on a 0.5 λ resolution grid.

III. THEORY AND IMPLEMENTATION

A. Data structure

The acquired beamformed image series (s) in-phase/ quadrature (IQ) data can be modelled as a linear mixture of tissue clutter signal (c), microbubble signal (b), and noise (n):

$$s(x, z, t, p) = c(x, z, t, p) + b(x, z, t, p) + n(x, z, t, p), \quad (1)$$

where x stands for the lateral dimension, z stands for the axial dimension, t stands for time, and p stands for transmitted pulse number. The clutter and noise signal need to be removed from the mixture in order to accurately assess the microbubble signal. A further property of the tissue clutter is that it dominates the images, over microbubble signal and noise, which is important as the filter described in the next sections order the signals partly based on their intensity.

B. Conventional processing

Conventionally, the MPCS suppress the linear tissue clutter signal by subtracting (AM) or summing (AMPI) the signals

backscattered from the complementary pulse transmissions (p). Two assumptions are made: (i) the tissue backscatter signal has a linear relationship with the phase and/or amplitude of the transmitted pulse, and (ii) negligible motion occurs within the time interval of the complementary pulse transmissions. When these assumptions hold then the residue in the processed signal consists of the nonlinear microbubble signal and noise. However, the contrast echocardiography signals violate the assumptions: Nonlinear ultrasound propagation in tissue also generates second-harmonic frequency content, that will give some residual signal in the linear combination of the complementary pulses that appears as tissue clutter in the contrast-enhanced images [5] and tissue motion induces signal misalignment that causes imperfect linear signal cancellation, leading to the generation of motion artifacts [10], [11].
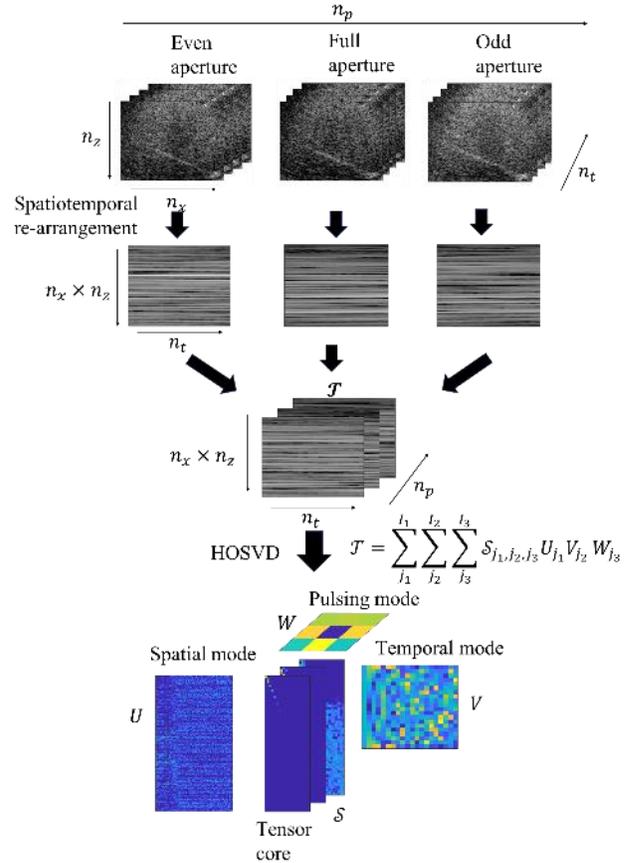
Fig. 2. Illustration of the tensor arrangement from stacks of ultrasound images and its decomposition with HOSVD.

C. Higher-order SVD processing rationale

Instead of linearly combining the complementary pulses, we propose to use HOSVD to retrieve the microbubble signal. HOSVD takes an nth order tensor as its input and decomposes it into a tensor core and n-orthogonal modes that each have individual ranks. We hypothesize that HOSVD is able to separate the clutter, microbubble, and noise signal, based on their different correlation of spatial, temporal, and the backscatter response (magnitude and phase) to the transmitted pulses. Just like in 2-D SVD, HOSVD decomposes the signal into all-orthogonal singular vectors and sorts them based on the magnitude of the multilinear singular value (MSV).

HOSVD is implemented on an ultrasound image series $s(x, z, t, p)$, arranged as a 3rd order tensor $\mathcal{T}(x \times z, t, p) \in \mathbb{C}^{x \cdot z \times t \times p}$, which represents spatial, temporal, and pulsing dimensions as the input. The 3rd order tensor $\mathcal{T}$ can be decomposed with HOSVD as:

$$\mathcal{T} = \mathcal{S} \cdot U \cdot V \cdot W,$$
$$= \sum_{j_1}^{I_1} \sum_{j_2}^{I_2} \sum_{j_3}^{I_3} \mathcal{S}_{j_1,j_2,j_3} U_{j_1} V_{j_2} W_{j_3}, \qquad (2)$$

where $\mathcal{S}$ is the core tensor with dimensions $\mathbb{C}^{x \cdot z \times t \times p}$, U is the spatial mode singular vectors, V is the temporal mode singular vectors, W is the pulsing mode singular vectors, and I_1, I_2, I_3 are the spatial, temporal, and pulsing mode component ranks, respectively. An example of re-arranging AM images and the resulting decomposition is shown in Fig. 2. Assuming that the clutter, microbubble, and noise are decomposed into different ranks, the filtering process is similar to the regular SVD filtering process, which is removing the ranks that mainly consist of clutter and noise. However, the tensor core is not diagonal like in regular SVD, but a 3rd order non sparse tensor, which means that every combination from all the modes has a particular tensor core value. As a result, unlike regular SVD that only requires a rank selection that applies for both spatial and temporal singular vectors, the rank selection for HOSVD has to be performed on each dimension separately.

D. Rank selection for clutter filtering

Each of the decomposed dimension represents different physical meaning; thus, every dimension needs a specific rank selection algorithm. It makes the rank selection more flexible and complicated at the same time. After the rank selections are performed, the HOSVD as a clutter filter to retrieve microbubble signal ($\hat{b}(x, z, t)$) can be implemented as:

$$\hat{b}(x, z, t) = \sum_{j_1 \in l_1} \sum_{j_2 \in l_2} \sum_{j_3 \in l_3} S_{j_1,j_2,j_3} U_{j_1} V_{j_2} W_{j3}, \qquad (3)$$

Where l_1, l_2 and, l_3 are the selected n-mode ranks for spatial, temporal, and pulsing mode, respectively. We developed different algorithms for the *in vitro* and *in vivo* data set as they have different conditions and complexity.

1) In vitro rank selection

a) Pulsing dimension

The scattered response of both tissue and microbubbles to the transmitted pulse is mostly linear, especially at the fundamental frequency like used in our experiments. However, microbubbles also generate 'non-linear fundamental' signals in response to the complementary transmitted pulses [4], [8], characterized by either non-linear amplitude, or amplitude-dependent phase response, or both; for our proposed technique, the exact cause is not important: This 'non-linear fundamental' component is different from the linear tissue response and hence will be decomposed into another rank than the linear

tissue rank. Since it is assumed that the linear responses will dominate the original data, the ranks with linear response will get the highest singular values, which means that they will appear in the first rank or ranks. The residual non-linear component or components will appear in the last rank since their overall magnitude is lower.
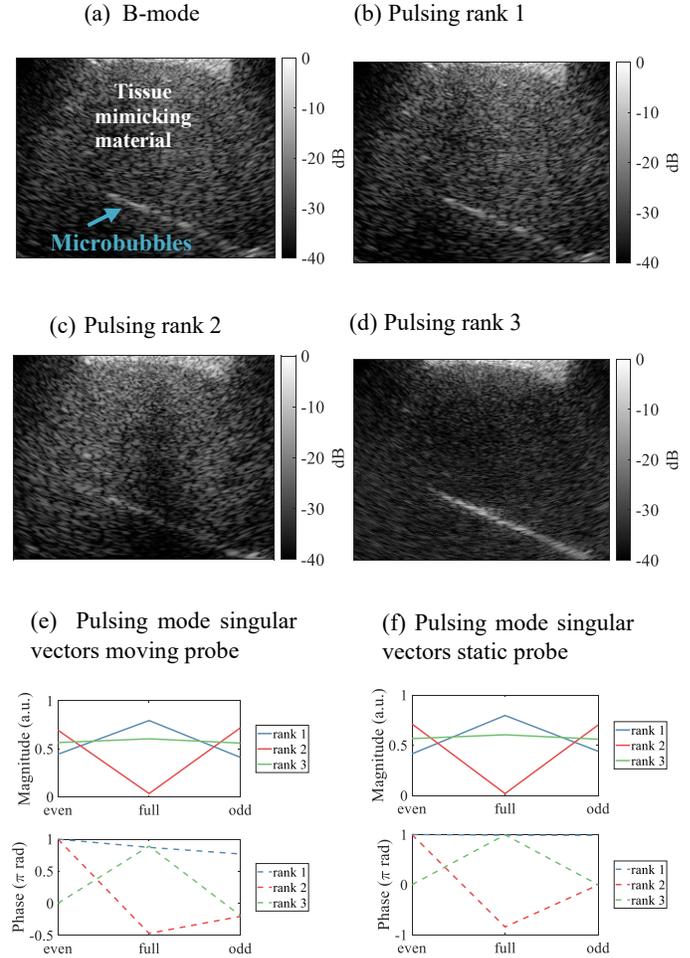
Fig. 3. (a) The B-mode image of the phantom as a reference. (b)-(d) The examples of ultrasound images as a result of pulsing mode rank selection. (e) and (f) The singular vectors that represent the backscatter trend, in response to the transmitted pulses (AM).

To exemplify the pulsing rank separation, ultrasound images are shown for each pulsing rank in Fig. 3 (b-d). Here, all the spatiotemporal ranks were kept for illustration. The pulsing mode singular vectors represent the backscatter response of the scatterers to the different transmission pulses ($W_{j3}(p)$), shown in Fig. 3(e). The first pulsing rank W_1 shows the major components of the magnitude and phase in response to the AM transmission. In this rank, the first (even) and third (odd) transmitted pulse each contain approximately half energy, and indeed the magnitude of the second response (full aperture) has twice the magnitude of the others and the phase is almost constant. The residual phase shift in the three responses originates from the overall motion of the probe. As a comparison, the phase of the first pulsing rank is constant when

the probe was static (Fig. 3. (f)). The reconstructed image of the first pulsing rank W_1 corresponds closely to the B-mode/fundamental imaging (Fig. 3. (a)). The second pulsing rank W_2 mostly has energy on the even and odd transmission. This can be explained by its correspondence to the residual difference between the even and odd-element transmissions: although the wavefields do overlap, there remains minor differences in their wavefronts since the elements by which the wavefield is transmitted are their mutual adjuncts (Fig. 3. (c)). Lastly, the third rank shows the total residual signal, that is mainly originating from nonlinear responses of microbubbles deviating from the general tissue and (linear) bubble responses, but can still contain noise. Indeed, the reconstructed image mainly shows the microbubble signal inside the target channel (Fig. 3. (d)). Thus, the clutter filtering for the pulsing dimension was performed by removing the first and second pulsing ranks as they predominantly consist of unwanted clutter signal.

b)   *Spatial dimension*

Like 2D-SVD, the spatial singular vectors $U^{x \cdot z \times t \cdot p}$ can be reshaped into ultrasonic spatial images $U^{x \times z \times t \cdot p}$. The manual distinction between the spatial mode singular vectors ($U_{j1}(x,z)$) that consist of clutter, microbubble, and noise signal is straightforward because they can simply be visualized. As shown in Fig. 4. (a), $U_7(x,z)$ and $U_9(x,z)$ visibly consist of microbubble signal. Accordingly, the clutter filtering should be performed by keeping those two ranks. A comparison between Fig. 4(a) and Fig. 4(b) shows that the spatial ranks with highest magnitude in pulsing rank 3 correspond to the images with highest visibility of the microbubble-containing channel. Thus, the automatic rank selection was performed by choosing the spatial ranks that have the highest magnitude. Thus, the automatic rank selection was performed by choosing the spatial ranks that have the highest magnitude, as well as those above the threshold of 0.4.

The microbubbles had negligible flow speed compared to the probe velocity, so we don't expect that the microbubble and tissue signal are decomposed into different temporal ranks. The temporal singular vectors ($V_{j2}(t)$) that represent the spectral variation of the signal and the MSV of the temporal mode are shown in Fig. 5. Since there was no separation between tissue and microbubble signal in the temporal dimension, all temporal singular vectors were kept for the *in vitro* data processing.

(a)   Spatial mode singular vectors

(b)   Spatial mode tensor core magnitude (pulsing rank 3)
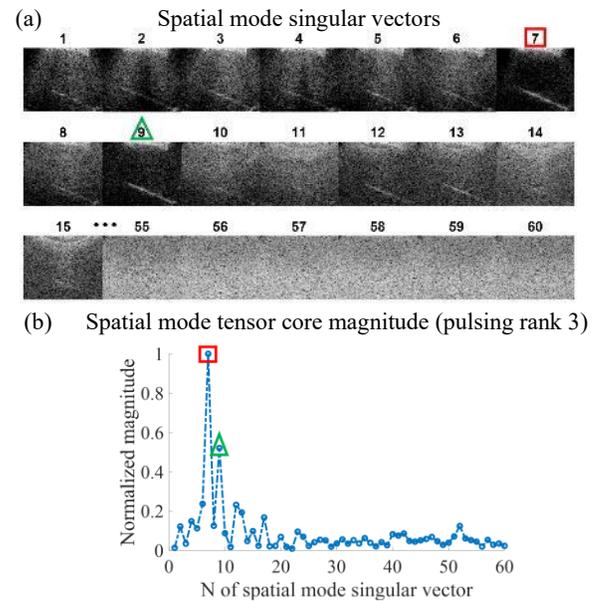
Fig. 4. (a). The spatial mode singular vectors, reshaped as ultrasound spatial images ($U(x,z)$). (b). The tensor core magnitude of the spatial singular vectors when only $W_3(p)$ is chosen.

Temporal mode singular vectors and values
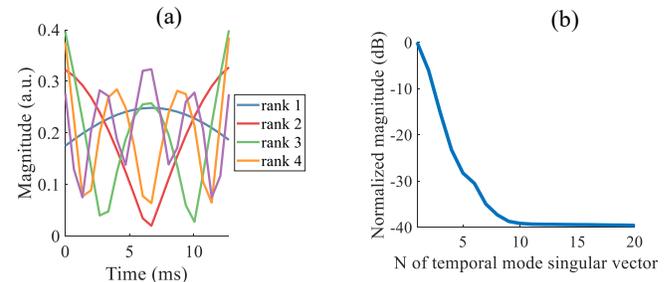
Fig. 5. (a) Modulus of the first four temporal singular vectors ($V_1(t) - V_4(t)$). (b). Normalized magnitude of the temporal mode MSV.

2)   *In-vivo rank selection*

a)   *Pulsing dimension*

Similar to the *in vitro* data, we expect the 'non-linear fundamental' microbubble signal to be decomposed into rank 3 of the pulsing mode vector ($W_3(p)$). As shown in Fig. 6., the pulsing mode singular vectors followed the same trend as the *in vitro* data-set. Yet, since AMPI was used in this specific example, the phase of the rank shifts by π between full and even/odd transmission. Moreover, the reconstructed *in vivo* images show the tissue responses for rank 1 and 2, and contrast signal in rank 3. Thus, the same rank selection was applied to the *in vivo* data set: keeping the 3rd pulsing rank.
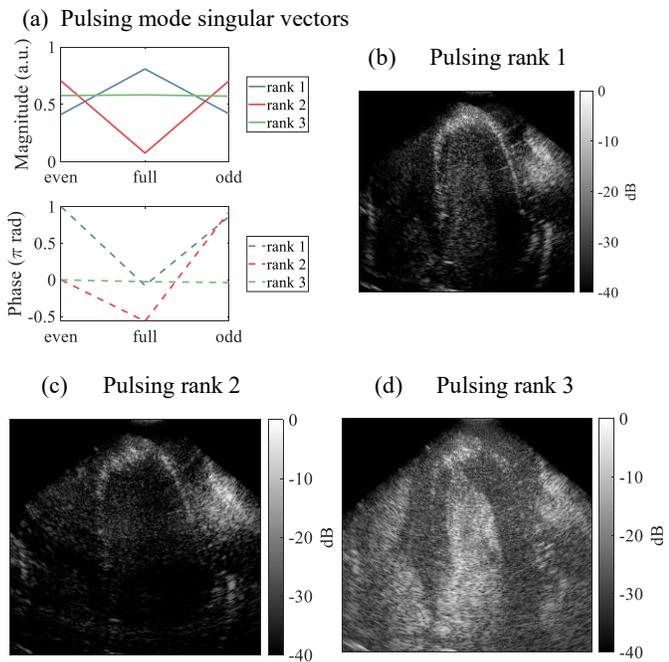
Fig. 6. (a). The singular vectors that represent the decomposed backscatter response to AMPI transmission (b)-(d) The examples of ultrasound images as a result of pulsing mode rank selection.

b)   Spatial Dimension

The spatial structure, as well as non-rigid motion, of the *in vivo* dataset is substantially more complex than the *in vitro* dataset. Unlike the *in vitro* spatial mode decomposition, the tensor core energy is widely spread across spatial singular vectors and there are no singular vectors that have significantly higher magnitude than the rest. As a result, the *in vitro* rank selection algorithm could not be applied straightforwardly.

Analogous to the regular 2D SVD, the ranks were sorted based on the total energy and the subspaces that contain residual tissue clutter signal mostly are allocated in the lower ranks, and those that contain microbubble signal mostly in the middle to high ranks. Since the spatial mode MSV have gradual changes, we expect that there is a detectable trend on the slope of the MSV when the rank subspaces change their dominant contents, similar to the regular SVD structure [25]. The gradient of the MSV is shown in Fig. 7. The local peaks of the derivative (rank 31) coincide with the transition of the subspaces, so it was chosen as the start of the selected ranks. Rank 15 was chosen as the start of the peak searching because empirically, we observed that the tissue subspace occupied more than the first 15 ranks. This value of 15 may depend on ensemble length and tissue motion, although we found that this value worked for both closed-chest data and open-chest data. All the subsequent ranks are selected with the assumption that microbubble signal, especially the 'non-linear fundamental' part has lower energy than the tissue signal and the spatial decomposition doesn't have ranks that only contain noise.
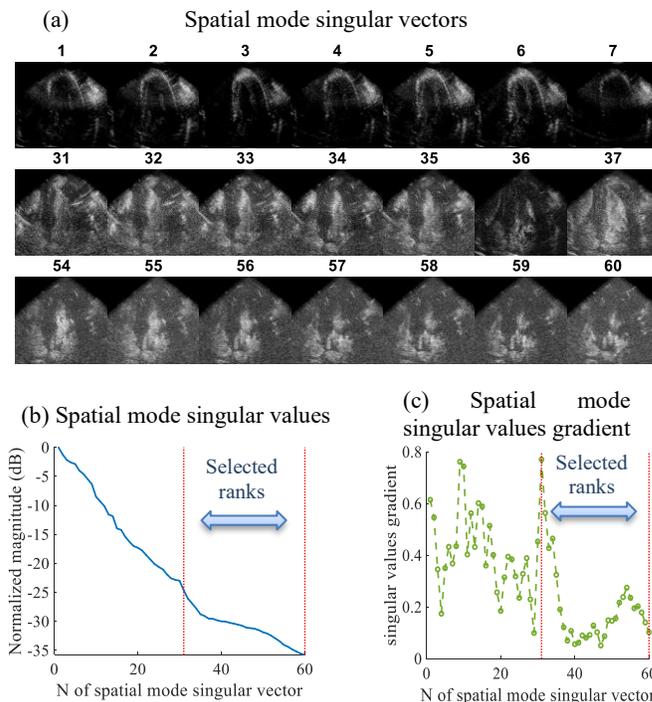


Fig. 7. (a). Representative ranks of the reshaped spatial mode singular vectors $(U_{j1}(x,z))$. (b). Normalized magnitude of the spatial MSV. (c). The gradient of the spatial MSV, the peak (rank 31) is chosen as the start of the selected ranks.

c)   Temporal Dimension

Different from the *in vitro* case, where the only flow of interest is within the channel, microbubble flow in the chambers of the heart is not negligible, and might influence the signal decomposition when filtering for perfusion in the heart walls. The microbubble flow peak velocity in the chambers is faster than the tissue motion and the coronary circulation also has wide range of flow velocity. Cardiac motion typically is non-rigid. All of these factors will cause the microbubble signal to appear in different ranks in the temporal dimension. Since we are interested in the slow flow in the myocardium and not the fast flow in the chamber and the fast tissue motion, rank selection can be performed on the temporal dimension.

The temporal singular vectors and their frequency contents are shown in Fig. 8. (a). It can be seen that the singular vectors corresponding with higher temporal ranks have increasing dominant frequency, with the first rank representing almost static motion and the last ranks representing mostly noise and aliased motion around the highest Doppler velocities. Since our interest mainly lies in detecting slow flow in the microcirculation, with velocities slower than 1 mm/s, we need to retain the lower ranks and discard the higher ones. We calculated the dominant (maximum) frequency of each rank (as shown in Fig. 8 (b)) and selected the ranks with a dominant frequency below 50 Hz, and the effect of this choice will also be demonstrated.
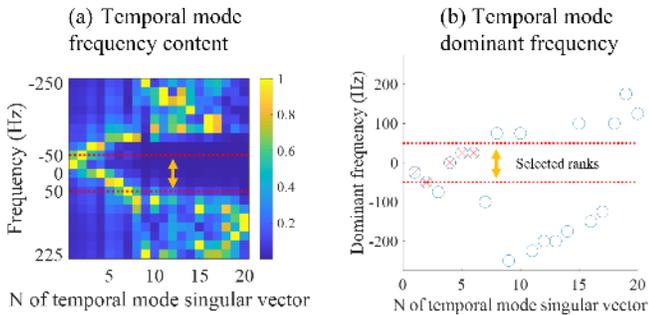
Fig. 8. (a). The frequency content of the temporal mode singular vectors. (b). The dominant frequency of each temporal mode singular vector and the selected low frequency ranks.

E. Postprocessing and Analysis

1) In vitro image quality quantification

HOSVD processing was performed on the beamformed quadrature demodulated data using the Tensorlab toolbox [26]. To quantify the efficacy of our proposed method, we implemented HOSVD with the rank selection method as mentioned above, and compared this with regular B-mode, conventional AM, and SVD spatiotemporal filter [14] on both the full-aperture transmit pulse and conventional AM. We performed our analysis during two scenarios: when the probe was static and when it was moving at a constant velocity of 35 mm/s. Each scenario consisted of a time interval of 200 ms (comprising 300 temporal frames). For both scenarios, HOSVD was implemented on an ensemble of 20 temporal frames (13.3 ms) with 10 samples temporal overlap. For the moving probe scenario, SVD was also implemented on an ensemble of 20 temporal frames, while all 300 frames were used for the static probe scenario to optimize tissue and flow separation [25]. The example of SVD rank selection is provided in the appendix. The Regions of interest (ROIs) were drawn on the channel (contrast) and PVA (background) to perform the quantitative analysis in the first frame (Fig. 9). The ROIs then automatically followed (using a 2D cross correlation-based global motion estimator) the channel and PVA while the probe was moving in subsequent frames. Contrast-to-background ratio (CBR) was then calculated to evaluate the filters' performances to suppress clutter signal, defined as $CBR_a = 20 \log_{10}\left(\frac{\overline{RMS}_{contrast}}{\overline{RMS}_{background}}\right)$, where $\overline{RMS}$ is the time-averaged root-mean-square signal strength in the time interval (200 ms). Overview box plots were calculated with: whiskers cover approximately 99% of the data; bottom and top of each box denote 1st and 3rd quartile of the data; solid lines in the middle of each box signify the data median.
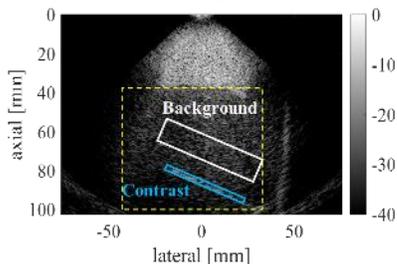

Fig. 9. Regions used for calculating CBR. The blue and white region used for contrast and background signal, respectively. The yellow region indicate the field of view to display the result of different filters.

2) In vivo image quality quantification

The three synthetic-aperture transmissions were coherently compounded on each pulse before HOSVD is implemented. Ensemble length of 20 temporal samples (40 ms) with 10 samples overlap was used for HOSVD clutter filtering. The performance of our proposed HOSVD filter was compared with the conventionally processed AM. Power Doppler was computed using $PD(z,x) = \sum_{t=1}^{T}|S(z,x,t)|^2$, where $S(z,x,t)$ are the filtered ultrasound images. The tissue suppression efficacy during motion was assessed on the open-chest acquisitions, using $CBR_p = 10 \log_{10}\left(\frac{\overline{RMS}_{contrast}}{\overline{RMS}_{background}}\right)$, in 75 temporal frames (150 ms) s in the ECG signal on Fig. 12 (e)). We use a factor of 10 in this equation as the contrast and background signal are power Doppler signals, i.e., already are squared values of the magnitude. In order to quantify this tissue suppression, we drew ROIs on the myocardium where no tissue clutter was visible and hence only showed contrast or noise signal and on the region where the residual tissue clutter due to motion was clearly observed - acting as background. The areas are shown in Fig. 10 (a).

The contrast detection efficacy on the closed-chest acquisition was assessed during end -diastole by calculating contrast ratio (CR) before and after FLASH sequence, calculated by $CR = 10 \log_{10}\left(\frac{\overline{RMS}_{pre-FLASH}}{\overline{RMS}_{post-FLASH}}\right)$. The ROI on the myocardium to compare the pre-FLASH and post-FLASH destruction sequence is shown in Fig. 10. (b).
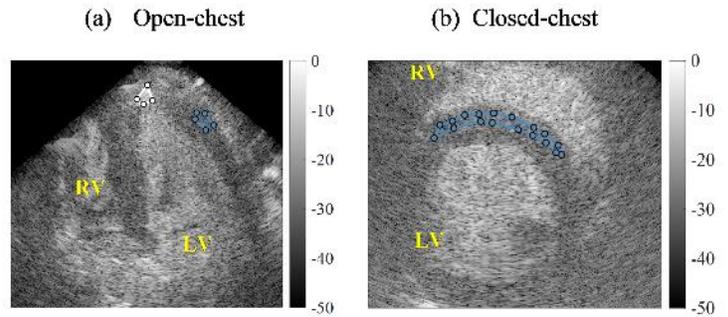
Fig. 10 (a). Regions used for calculating CBR in the cardiac measurements. The blue (myocardium) and white (epicardium) region used for contrast and background signal, respectively. (b). The blue region (myocardium) used for calculating contrast signal strength. LV and RV indicate left and right ventricle, respectively.

IV. RESULTS

A. In vitro

Representative phantom contrast images during motion (35 mm/s) are shown in Fig. 11. (a)-(d). The flow channel is visible in all images, yet, the background is most suppressed when using AM + HOSVD thus giving best visibility of the channel. When quantifying (Fig. 11. (f)), the CBR of HOSVD on AM exceeds that of the conventionally processed AM by 10dB, AM + SVD by 11dB, that of both SVD-filtered, and unfiltered by 14dB. During the time interval where the probe was not moving (images not shown for brevity), HOSVD

achieved 5dB, 4.5 dB, 12dB, and 17dB CBR improvement over conventional AM, AM + SVD, SVD filtered, and unfiltered images, respectively. See Fig. 11. (f) for these quantified results including their spread. The SVD-filtered images have worse CBR than the AM images or the AM + HOSVD. Note that SVD-based contrast filtering assumes that contrast agents signal is highly decorrelated with the tissue signal, i.e., has distinct motion. In this experiment that mimics perfusion and slow flow in relatively fast-moving cardiac tissue, such assumption is largely violated since the contrast agents have very low flow velocity in the channel, and, on top, they move with the tissue in the 'moving probe' experiment
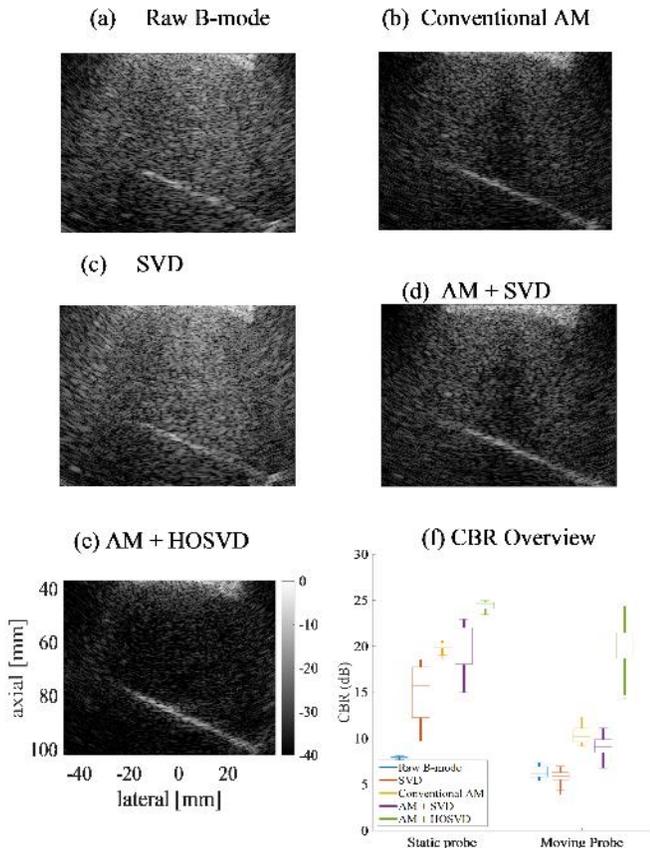
Fig. 11. (a) - (d). Representative contrast images of different processing during moving probe. (e). The CBR values overview, obtained with different processing filters and probe motion. The box plots represent median, 50% and 99% ranges.

B. In vivo

Representative power Doppler images of the open-chest acquisition (apical view) during early-diastole are shown in Fig. . Qualitatively, it can be observed that the HOSVD+AM images (Fig. 12. (b) and (d)) show more microbubble signal in the myocardium (cyan arrow) and more supressed tissue clutter signal (white arrow), compared to the conventionally processed AM images (Fig. 12. (a) and (c)). Quantitatively, HOSVD+AM provided 19 dB CBR improvement over the conventionally processed AM images. The ECG signal of the image period (40ms) are shown in Fig. 12.(e).

The example images from the closed-chest acquisition (parasternal short axis view) pre and post FLASH destruction

sequence, processed with different schemes are shown in Fig. 13. Compared to the open-chest apical view, the non-linear propagation artifact was more consequential in this view because the right ventricle (that contains a high concentration of microbubbles) was in the ultrasound propagation path. On the other hand, the motion artifacts might be expected to be less severe. These images show that the tissue signal is suppressed and microbubble signal can be seen inside the myocardium boundaries.

In the pre-FLASH-destruction images, the results of conventional AM processing, and HOSVD filtering with two temporal mode rank selection are shown in Fig. 13. To demonstrate the effect of the temporal mode rank selection (based on Fig. 13. (b).), images that represent low-rank signals (Fig. 13. (c).) and high-rank signals (Fig. 13. (d).) are displayed. We could identify a myocardial perfusion signal after low-rank HOSVD processing Fig. 13. (c), and visibly more compared to the conventional AM Fig. 13. (a)). On the contrary, the high-rank HOSVD (Fig. 13. (d)) procesesed image does not show microbubble signal inside the myocardium but more signal inside the left ventricle. These results show that HOSVD could separate the slow- and fast- moving microbubble signal. The images post-FLASH destruction sequence, processed with conventional AM and low-rank HOSVD Fig. 13. (e) and (f)) displays significantly less signal inside the myocardium; only a feeding vessel is observed, which can be expected right after the FLASH destruction pulses. It signifies that the detected signal on pre-FLASH images originate from microbubbles rather than tissue residuals. The signal strength ratio inside the myocardium region pre and post FLASH destruction sequence of the low-rank HOSVD processed images are 3dB higher than the conventional AM processing. It indicates that the HOSVD processing provides better contrast detection inside the myocardium.

V. DISCUSSION

In this study, we proposed to use higher-order singular value decomposition (HOSVD) as a method to process the complementary pulses of multi-pulse contrast sequences (MPCS) instead of conventionally summing or subtracting them. We expect HOSVD to improve contrast detection in case in the presence of motion, nonlinear propagation, and slow microbubble flow, where the commonly used conventional MPCS and spatiotemporal SVD are less effective. The results of both our *in vitro* and *in vivo* porcine heart model show that HOSVD provides superior contrast detection. In our flow phantom experiment, HOSVD exceeds conventional MPCS by 10 dB, AM + SVD by 11dB, and spatiotemporal SVD and unfiltered by 14dB each. In our *in vivo* open-chest implementation, HOSVD provides better motion artifact suppression than conventional MPCS by 19dB and improves

contrast detection in a trans-thoracic (closed-chest) experiment by 3dB.
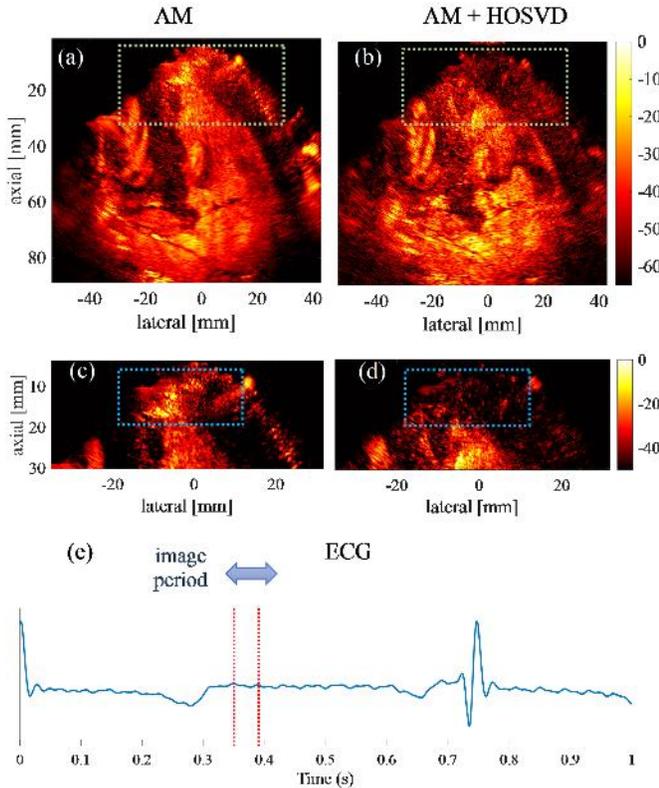
Fig. 12 Comparison of open-chest apical view AM images, processed conventionally and with HOSVD. The conventionally processed AMPI images (a) and (c) can be compared with the HOSVD-processed images (b) and (d), respectively. The tissue motion artifacts at the apex of the heart are more suppressed and microbubble signals could be seen better (cyan boxes) with HOSVD than the conventional processing.

HOSVD contrast detection improvement over conventional MPCS and SVD is more powerful in the case when motion artifacts exist. As shown by the results of our *in vitro* experiment, HOSVD provides 10 dB CBR improvement over AM when the probe is moving, compared to 5 dB improvement when the probe is static (where AM is generally working well in suppressing tissue signal). In the case of SVD, it has been reported that the spatiotemporal SVD filter's capability to detect flow is deteriorated when the flow speed is slower than the tissue motion velocity [14], [17], [18]. Hence, the nearly static microbubble flow in moving probe *in vitro* experiment and the *in vivo* and the myocardial perfusion are difficult cases for spatiotemporal SVD filtering because of the high spatio-temporal correlation between the microbubble and tissue signals when they are moving along. The improvement in contrast signal separation achieved by HOSVD over SVD becomes clear by comparing the spatial mode singular vectors of the two methods. As seen in the Method section, HOSVD was able to separate contrast and tissue signal into individual spatial components. On the other hand, SVD was not able to discriminate since all component still consists of a mixture of contrast and tissue signal (see Appendix), which make the filtering process unfeasible since no component or set of components could be selected that contains contrast signal only.

Consequently, the *in vitro* results show that SVD completely fails to separate the microbubble signal when the probe is moving since it provides the same CBR as in the unfiltered images, while HOSVD improved the CBR up to 17 dB Respectively, the CBR improvement in the open-chest *in vivo* results is due to the fact that HOSVD could better overcome the motion artifacts, compared to conventional AM processing. The tissue displacement (especially at the apex of the heart) caused signal misalignment when the pulses were summed (conventionally processed), and thus impaired tissue suppression. The SVD filter was also tested (not shown here) on the *in vivo* dataset but it only showed improvement of contrast visibility over AM during the brief moments where tissue was mostly still, and therefore using the SVD filtering technique would have limited useability in the clinical application of myocardial perfusion imaging.

Analogous to the regular 2D SVD filtering, HOSVD filter outcome is determined by the rank selection. Due to the
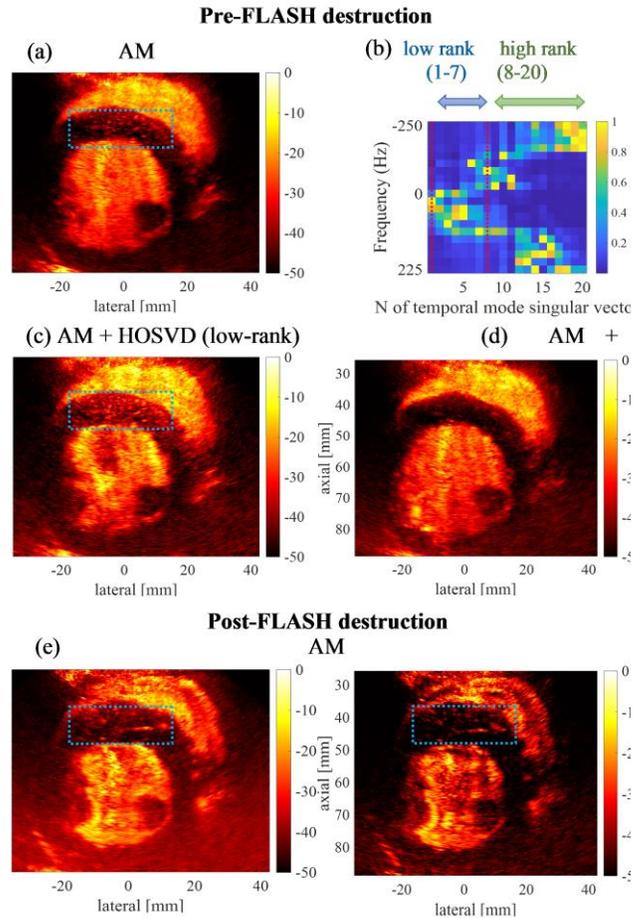
Fig. 13 (a), (c) – (f). Comparison of closed-chest parasternal short axis AM images, processed conventionally and with HOSVD. (b) The frequency contents of the temporal mode singular vectors and the rank selection. The image pre-FLASH destruction processed with (a) conventional AM shows less microbubble signal in the interventricular septum (cyan boxes) with the (c) low-rank HOSVD-processed image. (d) The high-rank HOSVD-processed HOSVD does not show microbubble signal inside the myocardium and more signal in the chamber because it does not have low frequency component in slow time. The images post-FLASH destruction of both processing (e) and (f) have much less microbubble signal in the interventricular septum.

different complexity of the images, we used different rank selection methods for spatial and temporal modes to process the *in vitro* and *in vivo* data. The rank selection for the pulsing ranks was straightforward in both our experiments: the last rank

contained most of the nonlinear bubble signals, for both AM and AMPI. In an additional test (not shown here), we applied HOSVD filtering on a pulse inversion data set and found again that taking the last rank -rank 2, in that case- showed most contrast. It is also worth to mention that the performance of HOSVD by rank selection on the pulsing mode is already better than the conventional pulse summation in the *in vitro* dataset and yields at least similar results for the *in vivo* dataset.

The spatial selection based on the tensor core magnitude pulsing mode rank 3 only works in the *in vitro* dataset. The tissue mimicking material (PVA) has a homogeneous and much simpler structure than the structure of a porcine heart. Furthermore, the motion emulated by the probe is rigid, while the cardiac motion field was complex. In the *in vitro* case the contrast-signal ranks were clearly visible both from the images as well as the rank magnitudes, thus easily facilitating the rank selection. In the *in vivo* case, the separation between tissue and contrast signal was not done into unique ranks, yet, a global cross-over point between the signals could be identified. The temporal selection that we adapted for the *in vivo* dataset worked well, yet it did continue on a fairly good separation of the microbubble and tissue response from selecting the last pulsing rank. We expect that the physiological tissue motion of the organ will, in the end, determine the algorithm: with limited and relatively uniform motion, the *in vitro* algorithm should be tested first, and with complex motion field, the *in vivo* algorithm. We performed temporal selection for the *in vivo* data to select perfusion, and by doing so, we removed some of the fast-moving bubble signal. *In vitro* temporal selection is not possible nor necessary because the microbubble inside the channel did not flow. Thus, its only motion was solely modulated by the rigid global motion. It should be noted that we adopted empirical threshold for choosing spatial ranks of both *in vitro* and *in vivo* methods. Although these values work for our data, they should be checked and adjusted for different ensemble length and motion.

The decomposition of HOSVD highly depends on the ensemble length of the temporal samples. The temporal length needs to be optimized according to the motion that occurs in the images. For *in vitro* data during probe motion, increasing the ensemble length from 5 to 20 temporal samples increased the resulting CBR by 1.5 dB. However, based on our empirical results, increasing the ensemble length even more does not improve the CBR further, so 20 temporal samples were chosen. A longer ensemble is potentially better when the probe is static; yet, 20 temporal samples already provide sufficient CBR. For the *in vivo* data, 20 temporal samples (180 total frames with 'checkerboard pattern' transmission and 3 synthetic sub aperture) was providing satisfactory results.

Contrast-to-background ratio (CBR) is an appropriate parameter to quantitatively assess the filter's performance in the *in vitro* data because the contrast and background regions are clearly located in different pixels. On the other hand, it is less obvious to determine contrast and background regions in our *in vivo* data since it can be expected that all tissue is well perfused in these healthy animals. For cardiac application, normally CBR is calculated by drawing the contrast region on the chamber [11] or a big vessel [16] that only contain microbubble signal and the background region is drawn on the myocardium. However, for assessing myocardial perfusion, the contrast is located inside the myocardium itself. Even after filtering, the myocardium still consists of both microbubble and tissue signal. This issue is alleviated for our open-chest images, because some part of the myocardium was predominantly consisting of tissue signal motion artifact. Thus, an ROI that represents tissue region can be drawn. However, it measures the filter performance to suppress tissue clutter instead of quantitatively assess the amount of myocardial perfusion. For closed-chest images, there was not any region that only consisted of tissue signal but it can be observed that the myocardium was predominantly consisting of only tissue signal, right after the FLASH destruction sequence. Thus, we drew one region on the myocardium and the contrast detection between HOSVD and MPCS was assessed by comparing the ratio between pre and post FLASH destruction pulses. There are several possible reasons why the quantitative improvement in the open-chest data (19dB) is significantly greater than that in the closed-chest data (3dB). Firstly, it is important to note that the parameters used to assess the two are different, with CBR being used to assess tissue suppression and CR being used to assess contrast detection. Secondly, in the open-chest acquisition, the unobstructed myocardium is located directly under the probe, whereas in the closed-chest acquisition, the myocardium is located 3-4 cm deeper and obstructed by layers of fat and nonlinear propagation of microbubbles in the right ventricle. Lastly, tissue motion in the open-chest (unbounded) heart in the apical view is faster than in the parasternal short axis, resulting in the amplitude modulation being less effective in suppressing tissue signals and allowing for greater improvement.

It should be noted that our HOSVD clutter filtering has some shortcomings. It is possible that some parts of the microbubble signal may be removed due to imperfect signal decomposition. In addition, the computation time for our HOSVD clutter filtering method is longer than that for 2-D SVD. In our *in vivo* data processing, it took 5.5 s to process an ensemble of 20 frames, as opposed to 0.25 s for 2-D SVD. However, it is important to mention that real-time processing is not an essential necessity for now, and therefore, the longer computation time is not a crucial issue and might later be achieved by code optimisation and/or parallelisation. Furthermore, our current implementation can still be improved. First, the spatial singular vectors that consist of microbubble signal mostly are not located in consecutive ranks. Thus, selecting a subspace of the spatial singular vectors means that some ranks that consist of tissue signal mostly would be kept thus reducing contrast to background. Clustering the ranks instead of selecting a range could be a solution. Second, the optimal ensemble length depends on the amount of motion that occur in the data. Adaptive ensemble length, tailored to the

This article has been accepted for publication in IEEE Transactions on Ultrasonics, Ferroelectrics, and Frequency Control. This is the author's version which has not been fully edited and content may change prior to final publication. Citation information: DOI 10.1109/TUFFC.2023.3316130

11   IEEE TRANSACTIONS ON ULTRASONICS, FERROELECTRICS, AND FREQUENCY CONTROL

amount of motion (cardiac phase) could improve the contrast detection. Third, the inclusion of more input dimensions like imaging frequency or coded pulsing might be investigated in the future, yet this would add even more complexity to the rank selection. Fourth, when using a probe that would have sufficient bandwidth to also allow second harmonic imaging, the data might be further filtered to isolate the second harmonic signal. Since our probe had limited bandwidth, we used the full fundamental band only. Fifth, anatomical cropping of the regions of interest from the overall cardiac images may result in better clutter suppression since less data needs to be decomposed into the limited number of ranks. However, we found that coarse manual segmentation led to loss of details in the images such as the exact border delineation which reduced our confidence in the interpretation of the contrast images. Automated segmentation may overcome this issue. Lastly, HOSVD could benefit from an implementation of pre-filter tissue motion compensation because the tissue signal would be more coherent and longer ensemble lengths could be adopted. we expect that the *in vivo*-data decomposition will resemble more the the *in vitro*-data decomposition and associated simpler and better contrast signal isolation. To reach that aim, the motion should be corrected while preserving the local tissue phase information such as achieved by e.g. the Lagrangian beamformer by Cormier *et al.* [27]"

One further step of using the high frame rate imaging might be actual tracking of the contrast agent microbubbles, e.g. during the first filling of the vessels after FLASH destruction, which would provide further insight in flow velocities in the vessels independent of their flow direction. Such tracking might be applied using the recent ultrasound localisation techniques; the proposed filter can be used to initially suppress the tissue clutter. In current clinical use of CE, time-intensity curves of FLASH-replenishment tests are regularly used to assess local perfusion. We showed that at least in *in vitro* experiments our technique is more robust to motion than the other methods. Yet, we expect that the robustness to motion *in vivo* is not sufficient to fully avoid cyclic patterns in the TICs, and cardiac gating might still be preferred while analysing FLASH-replenishment tests.

VI. CONCLUSION

We have presented the application of higher-order SVD on multi-pulse contrast sequences to improve contrast detection in ultrafast ultrasound imaging. Both our *in vitro* and *in vivo* assessment has demonstrated that our proposed implementation provides superior contrast detection over the conventional processing scheme in MPCS, and the more recent spatiotemporal SVD filter. The improvement could give more confidence in detecting microbubble even in case of mild tissue motion and visualizing flow in the coronary circulation.

APPENDIX

Examples of SVD rank selection when spatiotemporal SVD was implemented on moving probe images. Low ranks with high spatial correlation were selected. However, SVD was

unable separate tissue and microbubble signals in both the implementation of full aperture transmission and AM images.
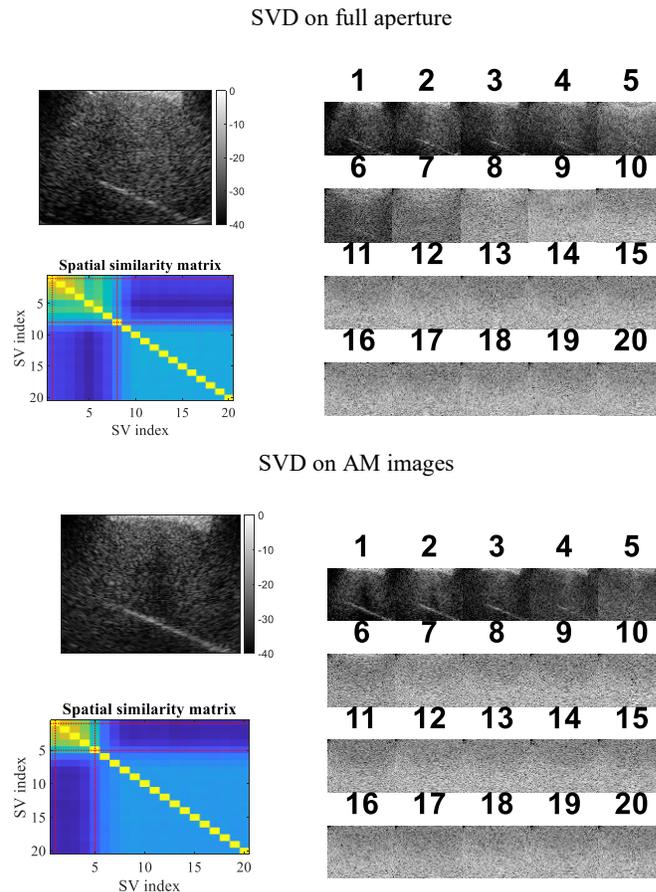
SVD on full aperture

SVD on AM images

REFERENCES

[1] R. Senior *et al.*, "Clinical practice of contrast echocardiography: Recommendation by the European Association of Cardiovascular Imaging (EACVI) 2017," *Eur. Heart J. Cardiovasc. Imaging*, vol. 18, no. 11, p. 1205, Nov. 2017, doi: 10.1093/ehjci/jex182.

[2] M. Strachinaru and F. J. ten Cate, "Microbubble Enhanced Echocardiography in Current Cardiology Practice," *Rev. Cardiovasc. Med.*, vol. 23, no. 6, p. 202, May 2022, doi: 10.31083/J.RCM2306202/FA868A15FA9B2534909E84510 1B3EB25.PDF.

[3] M. Dewey *et al.*, "Clinical quantitative cardiac imaging for the assessment of myocardial ischaemia," *Nat. Rev. Cardiol.*, vol. 17, no. 7, pp. 427–450, 2020, doi: 10.1038/s41569-020-0341-8.

[4] M. A. Averkiou, M. F. Bruce, J. E. Powers, P. S. Sheeran, and P. N. Burns, "Imaging Methods for Ultrasound Contrast Agents," *Ultrasound in Medicine and Biology*, vol. 46, no. 3.

This article has been accepted for publication in IEEE Transactions on Ultrasonics, Ferroelectrics, and Frequency Control. This is the author's version which has not been fully edited and content may change prior to final publication. Citation information: DOI 10.1109/TUFFC.2023.3316130

12   IEEE TRANSACTIONS ON ULTRASONICS, FERROELECTRICS, AND FREQUENCY CONTROL

Elsevier USA, pp. 498–517, Mar. 01, 2020, doi: 10.1016/j.ultrasmedbio.2019.11.004.

[5]   M. A. Averkiou, "Tissue harmonic ultrasonic imaging," *Comptes Rendus l'Academie des Sci. - Ser. IV Physics, Astrophys.*, vol. 2, no. 8, pp. 1139–1151, 2001, doi: 10.1016/S1296-2147(01)01259-8.

[6]   D. H. Simpson, C. T. Chin, and P. N. Burns, "Pulse Inversion Doppler : A New Method for Detecting Nonlinear Echoes from Microbubble Contrast Agents," *372 ieee Trans. Ultrason. Ferroelectr. Freq. Control*, vol. 46, no. 2, pp. 372–382, 1999.

[7]   G. A. Brock-Fisher, "Means for increasing sensitivity in non-linear ultrasound imaging systems," *J. Acoust. Soc. Am.*, vol. 101, no. 6, p. 3240, Jun. 1997, doi: 10.1121/1.418339.

[8]   P. J. Phillips, "Contrast pulse sequences (CPS): Imaging nonlinear microbubbles," in *Proceedings of the IEEE Ultrasonics Symposium*, 2001, vol. 2, pp. 1739–1745, doi: 10.1109/ultsym.2001.992057.

[9]   M.-X. Tang, N. Kamiyama, and R. J. Eckersley, "Effects of Nonlinear Propagation in Ultrasound Contrast Agent Imaging," *Ultrasound Med. Biol.*, vol. 36, no. 3, pp. 459–466, Mar. 2010, doi: 10.1016/J.ULTRASMEDBIO.2009.11.011.

[10]   C. Tremblay-Darveau *et al.*, "The role of microbubble echo phase lag in multipulse contrast-enhanced ultrasound imaging," *IEEE Trans. Ultrason. Ferroelectr. Freq. Control*, vol. 65, no. 8, pp. 1389–1401, Aug. 2018, doi: 10.1109/TUFFC.2018.2841848.

[11]   A. Stanziola *et al.*, "Motion Artifacts and Correction in Multi-Pulse High Frame Rate Contrast Enhanced Ultrasound," *IEEE Trans. Ultrason. Ferroelectr. Freq. Control*, vol. 66, no. 2, pp. 2019–2022, 2018, doi: 10.1109/TUFFC.2018.2887164.

[12]   A. Heimdal and H. Torp, "Ultrasound Doppler Measurements of Low Velocity Blood Flow: Limitations Due to Clutter Signals from Vibrating Muscles," *IEEE Trans. Ultrason. Ferroelectr. Freq. Control*, vol. 44, no. 4, p. 873, 1997.

[13]   O. Couture, M. Fink, and M. Tanter, "Ultrasound contrast plane wave imaging," *IEEE Trans. Ultrason. Ferroelectr. Freq. Control*, vol. 59, no. 12, pp. 2676–2683, 2012, doi: 10.1109/TUFFC.2012.2508.

[14]   C. Demené *et al.*, "Spatiotemporal Clutter Filtering of Ultrafast Ultrasound Data Highly Increases Doppler and fUltrasound Sensitivity," *IEEE Trans. Med. Imaging*, vol. 34, no. 11, pp. 2271–2285, 2015, doi: 10.1109/TMI.2015.2428634.

[15]   Y. Desailly, A. M. Tissier, J. M. Correas, F. Wintzenrieth, M. Tanter, and O. Couture, "Contrast enhanced ultrasound by real-time spatiotemporal filtering of ultrafast images," *Phys. Med. Biol.*, vol. 62, no. 1, pp. 31–42, 2017, doi: 10.1088/1361-6560/62/1/31.

[16]   J. Voorneveld *et al.*, "High-frame-rate contrast-enhanced ultrasound for velocimetry in the human abdominal aorta," *IEEE Trans. Ultrason. Ferroelectr. Freq. Control*, vol. 65, no. 12, pp. 2245–2254, 2018, doi: 10.1109/TUFFC.2018.2846416.

[17]   J. Zhu *et al.*, "High Frame Rate Contrast-Enhanced Ultrasound Imaging for Slow Lymphatic Flow: Influence of Ultrasound Pressure and Flow Rate on Bubble Disruption and Image Persistence," *Ultrasound Med. Biol.*, vol. 45, no. 9, pp. 2456–2470, 2019, doi: 10.1016/j.ultrasmedbio.2019.05.016.

[18]   G. Wahyulaksana *et al.*, "Independent Component Analysis Filter for Small Vessel Contrast Imaging During Fast Tissue Motion," *IEEE Trans. Ultrason. Ferroelectr. Freq. Control*, vol. 69, no. 7, pp. 2282–2292, Jul. 2022, doi: 10.1109/TUFFC.2022.3176742.

[19]   A. Thorstensen, H. Dalen, B. H. Amundsen, and A. Støylen, "Peak systolic velocity indices are more sensitive than end-systolic indices in detecting contraction changes assessed by echocardiography in young healthy humans," *Eur. J. Echocardiogr.*, vol. 12, no. 12, pp. 924–930, Dec. 2011, doi: 10.1093/EJECHOCARD/JER178.

[20]   L. De Lathauwer, B. De Moor, and J. Vandewalle, "A multilinear singular value decomposition," *SIAM J. Matrix Anal. Appl.*, vol. 21, no. 4, pp. 1253–1278, 2000, doi: 10.1137/S0895479896305696.

[21]   M. Kim, C. K. Abbey, J. Hedhli, L. W. Dobrucki, and M. F. Insana, "Expanding Acquisition and Clutter Filter Dimensions for Improved Perfusion Sensitivity," *IEEE Trans. Ultrason. Ferroelectr. Freq. Control*, vol. 64, no. 10, pp. 1429–1438, Oct. 2017, doi: 10.1109/TUFFC.2017.2719942.

[22]   G. Shechter, J. R. Resar, and E. R. McVeigh, "Displacement and velocity of the coronary arteries: Cardiac and respiratory motion," *IEEE Trans. Med. Imaging*, vol. 25, no. 3, pp. 369–375, Mar. 2006, doi: 10.1109/TMI.2005.862752.

[23]   C. Papadacci, M. Pernot, M. Couade, M. Fink, and M. Tanter, "High-contrast ultrafast imaging of the heart," *IEEE Trans. Ultrason. Ferroelectr. Freq. Control*, vol. 61, no. 2, pp. 288–301, 2014, doi: 10.1109/TUFFC.2014.6722614.

[24]   A. Rodriguez-Molares *et al.*, "The UltraSound ToolBox," Oct. 2017, doi: 10.1109/ULTSYM.2017.8092389.

[25]   D. Maresca, M. Correia, M. Tanter, B. Ghaleh, and M. Pernot, "Adaptive spatiotemporal filtering for Coronary Ultrafast Doppler Angiography," *IEEE Trans. Ultrason. Ferroelectr. Freq. Control*, vol. 65, no. 11, pp. 2201–2204, 2018, doi: 10.1109/TUFFC.2018.2870083.

[26]   N. Vervliet, O. Debals, L. Sorber, M. Van Barel, and L. De Lathauwer, "Tensorlab 3.0," *Available online.*, 2016, [Online]. Available: http://www.tensorlab.net.

[27]   P. Cormier, J. Poree, C. Bourquin, and J. Provost, "Dynamic Myocardial Ultrasound Localization Angiography," *IEEE Trans. Med. Imaging*, 2021, doi: 10.1109/TMI.2021.3086115.